PROCEEDINGS OF SCIENCE

The spectral reconstruction of inclusive rates

John Bulava [a,*]

[a] *Deutsches Elektronen-Synchrotron DESY, Platanenallee 6, 15738 Zeuthen, Germany*

E-mail: john.bulava@desy.de

A recently re-discovered variant of the Backus-Gilbert algorithm for spectral reconstruction enables the controlled determination of smeared spectral densities from lattice field theory correlation functions. A particular advantage of this approach is the *a priori* specification of the kernel with which the underlying spectral density is smeared, allowing for variation of its peak position, smearing width, and functional form. If the unsmeared spectral density is sufficiently smooth in the neighborhood of a particular energy, it can be obtained from an extrapolation to zero smearing-kernel width at fixed peak position. A natural application for this approach is scattering processes summed over all hadronic final states. As a proof-of-principle test, an inclusive rate is computed in the two-dimensional O(3) sigma model from a two-point correlation function of conserved currents. The results at finite and zero smearing radius are in good agreement with the known analytic form up to energies at which 40-particle states contribute, and are sensitive to the 4-particle contribution to the inclusive rate. The straight-forward adaptation to compute the R-ratio in lattice QCD from two-point functions of the electromagnetic current is briefly discussed.

The 39th International Symposium on Lattice Field Theory,
8th-13th August, 2022,
Rheinische Friedrich-Wilhelms-Universität Bonn, Bonn, Germany

*Speaker

PoS(LATTICE2022)231

1. Introduction

Lattice QCD simulations proceed by computing n-point euclidean correlation functions of (quasi-) local interpolating operators. Single-hadron states and finite-volume few-hadron states are isolated from correlation functions in the asymptotic large euclidean time limit. However, some hadronic phenomena are best studied by other means. As an example, this work considers inclusive rates defined as a sum over all hadronic final states produced by an external current. At large center-of-mass energies, a finite-volume approach to such a process is impractical since it requires the isolation of all individual finite-volume levels with arbitrarily many particles. Such processes are a cornerstone of QCD and connect the low-energy hadronic and high-energy perturbative regimes [1], serving as a manifestation of 'quark-hadron duality' [2] whereby perturbative QCD in terms of quarks and gluons becomes increasingly effective at computing inclusive rates summed over final states consisting entirely of hadrons.

For concreteness, consider the QCD part of the process $e^+e^- \to$ hadrons

$$\rho(s) = \frac{R(s)}{12\pi^2}, \quad R(s) = \frac{\sigma\left[e^+e^- \to \text{hadrons}\right](s)}{4\pi\alpha_{\text{em}}(s)^2/(3s)}, \tag{1}$$

$$\rho_{\mu\nu}(k) = \frac{1}{2\pi}\int d^4x\, e^{-ik\cdot x}\langle\Omega|\hat{j}^{\text{em}}_\mu(x)\,\hat{j}^{\text{em}}_\nu(0)|\Omega\rangle = (g_{\mu\nu}k^2 - k_\mu k_\nu)\,\rho(k^2), \tag{2}$$

where $\hat{j}^{\text{em}}_\mu$ is the quark-level electromagnetic current. The desired inclusive rate is given by the spectral density $\rho(s)$, which is also present in the analogous infinite-volume Euclidean correlator

$$C(t) = \int d^3\boldsymbol{x}\,\langle\Omega|\hat{j}^{\text{em}}_z(\boldsymbol{x})\,e^{-\hat{H}t}\,\hat{j}^{\text{em}}_z(0)^\dagger|\Omega\rangle = \int_0^\infty d\omega\,\omega^2\rho(\omega^2)\,e^{-\omega t}\,. \tag{3}$$

The direct determination of $\rho(s)$ in lattice QCD is not straightforward, however. First, the inversion of integral equations like Eq. 3 using $C(t)$ evalutated at a finite number of discrete times with statistical errors is notoriously ill-posed. Furthermore, the finite volume introduces additional complication. Even if the inverse problem were solved successfully and the finite-volume euclidean correlator $C_L(t)$ used to determine its spectral density $\rho_L(s)$, it differs qualitatively from its infinite-volume counterpart $\rho(s)$. While $\rho_L(s)$ is a sum over Dirac δ-functions for each finite-volume state, $\rho(s)$ is smooth apart from non-analyticities due to the opening of thresholds. In no way does $\rho_L(s)$ 'approach' $\rho(s)$ as $L \to \infty$.

The bridge between finite and infinite volume is made more effectively using the smeared spectral density

$$\rho_\epsilon(E) = \int_0^\infty d\omega\,\delta_\epsilon(E-\omega)\,\rho(\omega)\,, \tag{4}$$

where $\lim_{\epsilon\to 0}\delta_\epsilon(x) = \delta(x)$, $\delta(x)$ is the Dirac-delta function, and $\int_{-\infty}^{\infty} dx\,\delta_\epsilon(x) = 1$. This solves (in principle) both of the difficulties mentioned above: the inverse problem can be made arbitrarily mild by increasing in the smearing width ϵ and $\rho_{L,\epsilon}(E)$ approaches its infinite-volume counterpart in a well-defined manner. The goal is now to take the ordered double limit [3]

$$\rho(E) = \lim_{\epsilon\to 0^+}\lim_{L\to\infty}\rho_{L,\epsilon}(E), \tag{5}$$

the asymptotic corrections to which are discussed in Sec. 2[1].

Although spectral reconstruction has a long history in lattice QCD, particularly at finite temperature [4], the treatment of the inverse problem in Eq. 3 demands special care. In order to define the result of the spectral reconstruction procedure, precise knowledge of the smearing kernel in Eq. 4 is required. As detailed in Sec. 2, the Backus-Gilbert approach [5, 6] is suitable in this respect[2]. Since the estimator for the smeared spectral density $\hat{\rho}_\epsilon(E)$ is simply a linear combination of the input correlator data $\hat{\rho}_\epsilon(E) = \sum_t g_t(\epsilon, E)C(t)$, the resultant smearing kernel is given by the same linear combination of decaying exponentials in Eq. 3

$$\hat{\rho}_\epsilon(E) = \int d\omega\, \hat{\delta}_\epsilon(E,\omega)\,\rho(\omega), \qquad \hat{\delta}_\epsilon(E,\omega) = \sum_t g_t(\epsilon,E)\omega^2 e^{-\omega t}. \tag{6}$$

Explicit knowledge of $\hat{\delta}_\epsilon(E,\omega)$ is a minimum requirement for a well-defined spectral reconstruction procedure.

Naively the Backus-Gilbert approach provides knowledge of the kernel in Eq. 6 only *a posteriori* for a given choice of coefficients. However, the coefficients themselves can be chosen to approximate a particular smearing kernel specified *a priori* [9]. This important innovation is employed here and was applied to lattice field theory for the first time in Ref. [10]. In order to understand this reconstruction algorithm, and in particular demonstrate control over the systematic errors, a test in a controlled context is warranted. Such a test has been performed in Ref. [11] for the two-dimensional O(3) sigma model together with attempts at saturating the ordered double limit of Eq. 5.

The remainder of this work is organized as follows. The spectral reconstruction method is presented in Sec. 2 in the context of the O(3) model test mentioned above. Prospects for adapting the method to current correlators in lattice QCD is discussed in Sec. 3 and Sec. 4 concludes.

2. O(3) model test

This section reviews a spectral reconstruction test which was recently published in Ref. [11]. It employs the spectral reconstruction procedure of Ref. [10] in the two-dimensional O(3) sigma model. Consider the standard lattice discretization

$$S[\sigma] = \frac{\beta}{2}\sum_{x\in\Lambda} a^2 \sum_\mu \hat{\partial}_\mu\sigma(x)\cdot\hat{\partial}_\mu\sigma(x) = \beta\sum_{x\in\Lambda}\sum_\mu\left[1-\sigma(x)\cdot\sigma(x+a\hat{\mu})\right], \tag{7}$$

where $\sigma(x)\in\mathbb{R}^3$, $|\sigma(x)|=1$, and $\hat{\partial}_\mu f(x) = \frac{1}{a}[f(x+a\hat{\mu})-f(x)]$. This model has a conserved current

$$j^a_\mu(x) = \beta\epsilon^{abc}\sigma^b(x)\hat{\partial}_\mu\sigma^c(x) \tag{8}$$

at finite lattice spacing, and possesses a dynamically-generated mass gap m. The total zero spatial momentum euclidean current-current correlation function analogous to Eq. 3 (but without the factor

[1]Finite lattice spacing effects must also be removed by taking the continuum limit, which is here performed at fixed ϵ and E.

[2]Another spectral reconstruction algorithm for which the smearing kernel is formally known *a posteriori* is the Chebyshev polynomial approach of Ref. [7]. Ref. [8] compares that approach to the one employed here.

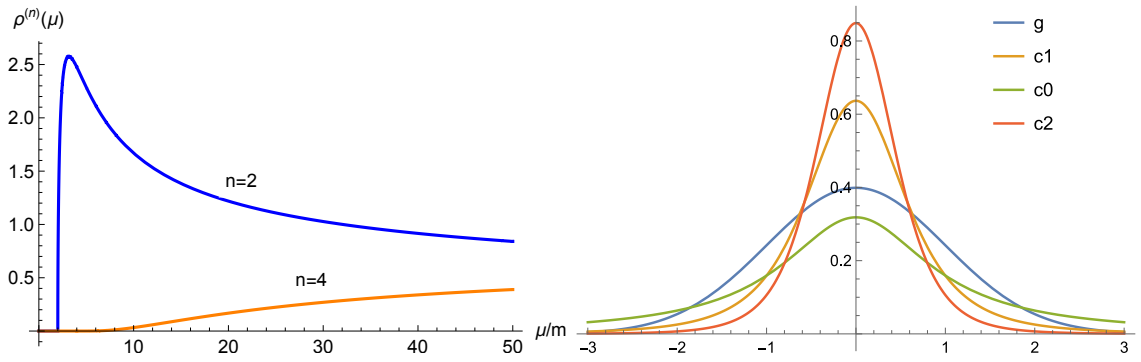

Figure 1: **Left**: exactly known $n = 2$ and $n = 4$ particle contributions to the (continuum, infinite-volume) spectral density associated with the conserved current in the two-dimensional O(3) sigma model. Contributions from states with more particles are insignificant in the energy range shown here. **Right**: the four smearing kernels $\delta^{\mathsf{x}}_{\epsilon}(x)$, where $\mathsf{x} = \{\mathsf{g}, \mathsf{c0}, \mathsf{c1}, \mathsf{c2}\}$, defined in Eq. 9 plotted against x with $\epsilon = 1$.

of ω^2) is computed by numerical simulations using the single-cluster algorithm of Ref. [12]. A variety of ensembles are generated, with $mL \approx 30 - 60$ and $am \in [0.01, 0.04]$ to assess finite volume effects and take the continuum limit. In the continuum the contributions to the associated spectral density $\rho(\omega)$ from each fixed-particle number sector can be computed exactly [13]. Below energies $E < 50m$, only the $n = 2$ and $n = 4$ particle contributions are significant and are shown in Fig.1.

In order to demonstrate the *a priori* specification of the smearing kernel, consider four kernels with different profiles as a function of $x = E - \omega$:

$$\delta^{\mathsf{g}}_{\epsilon}(x) = \frac{1}{\sqrt{2\pi}\epsilon}\exp\left[-\frac{x^2}{2\epsilon^2}\right], \qquad \delta^{\mathsf{c0}}_{\epsilon}(x) = \frac{1}{\pi}\frac{\epsilon}{x^2+\epsilon^2}, \tag{9}$$

$$\delta^{\mathsf{c1}}_{\epsilon}(x) = \frac{2}{\pi}\frac{\epsilon^3}{(x^2+\epsilon^2)^2}, \qquad \delta^{\mathsf{c2}}_{\epsilon}(x) = \frac{8}{3\pi}\frac{\epsilon^5}{(x^2+\epsilon^2)^3}, \tag{10}$$

including the gaussian (denoted 'g') and three Cauchy-like kernels denoted '$\mathsf{c}n$', for which $n = 0, 1, 2$ distinguishes the power of the pole. These kernels are depicted in Fig. 1.

The method advocated in Ref. [10] to reconstruct the smeared spectral density $\rho^{\mathsf{x}}_{\epsilon}(E)$, where $\mathsf{x} = \{\mathsf{g}, \mathsf{c0}, \mathsf{c1}, \mathsf{c2}\}$, is based on two criteria. First, the reconstructed smearing kernel $\hat{\delta}^{\mathsf{x}}_{\epsilon}(E, \omega)$ should be close to the desired one $\delta^{\mathsf{x}}_{\epsilon}(E - \omega)$. Second, the coefficients $\{g_t(\epsilon, E)\}$ in Eq. 6 should not induce a large statistical variance on the estimator $\hat{\rho}^{\mathsf{x}}_{\epsilon}(E)$. These two considerations are encoded in the functionals

$$A[g] = \int_{E_0}^{\infty} d\omega \, \left\{\delta^{\mathsf{x}}_{\epsilon}(E-\omega) - \hat{\delta}^{\mathsf{x}}_{\epsilon}(E,\omega)\right\}^2, \tag{11}$$

$$B[g] = \mathrm{Var}[\hat{\rho}^{\mathsf{x}}_{\epsilon}(E)] = \sum_{tt'} g_t(\epsilon, E)\, g_{t'}(\epsilon, E)\, \mathrm{Cov}[C(t), C(t')] \tag{12}$$

respectively. The coefficients are then chosen to minimize the combination functional $G_\lambda[g] = (1-\lambda)A[g]/A[0] + \lambda B[g]$, where the 'trade-off' parameter λ is introduced. For small λ, the 'accuracy' functional $A[g]$ takes preference over the 'precision' one $B[g]$ resulting in small systematic but large

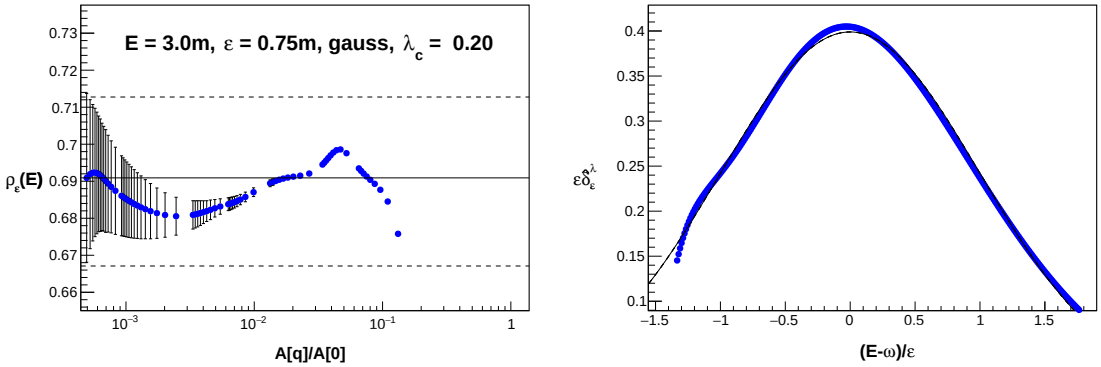

Figure 2: Left: indicative illustration of the trade-off between statistical and systematic errors for a particular choice of E and ϵ on a single ensemble. Each point corresponds to a different λ and the horizontal band indicates the chosen reconstruction (with $\lambda = \lambda_c = 0.20$) for which statistical errors dominate systematic ones. **Right**: for this same setup and $\lambda = \lambda_c$, the reconstructed kernel $\hat{\delta}^{\mathrm{g}}_{\epsilon}(E,\omega)$, together with the desired kernel $\delta^{\mathrm{g}}_{\epsilon}(E-\omega)$ shown as a solid line. All reconstructions employ the correlator timeslices $t = 1a, \ldots, 160a$.

statistical errors. By contrast, large λ results in small statistical errors but a reconstructed smearing kernel which does not resemble the desired one. The choice of the parameter λ is performed automatically and results in an approximate balance of these two criteria. The effect of varying λ is illustrated in Fig. 2 together with the reconstructed kernel $\hat{\delta}^{\mathrm{g}}_{\epsilon}(E,\omega)$ for a sample setup. The trade-off between statistical and systematic errors is familiar to lattice field theorists and the left panel of Fig. 2 resembles the identification of a plateau in effective mass plots.

The procedure described above is performed for a variety of E and ϵ, and for all four smearing kernels. Next, finite volume effects must be assessed and the continuum limit taken independently for each E, ϵ, and kernel. Finite-volume effects are assessed at a single lattice spacing by simulating two additional ensembles with doubled spatial and temporal extents, respectively. The differences $\Delta_{L,T}$ between the spectral reconstruction on the doubled lattices divided by the statistical error are shown in Fig. 3, which show (at most) moderately significant hints for finite-L effects at energies near the two-particle production threshold.

With the finite-volume effects demonstrably controlled for the (E, ϵ) values and the kernels in question, the continuum limit can be investigated. Cutoff effects for 'on-shell' quantities in the two-dimensional O(3) sigma model have a long history, due to their apparently linear behaviour which is caused by large logarithmic corrections [14]. Unfortunately, the analysis there is incomplete for the 'off-shell' smeared spectral density considered here. In order to explore the influence of logarithmic cutoff effects, the fit forms

$$Q(a) = Q(0) + Ca^2\beta^r, \qquad r = 0,\ 3,\ 6 \tag{13}$$

are explored to extrapolate the smeared spectral densities to the continuum limit. A comparison of the extrapolation forms is shown in Fig. 4. The continuum limits are generally mild and well-constrained by the data, although the slope becomes steeper for increasing E.

Given the assessment of systematic errors due to spectral reconstruction, finite L and T effects, and finite lattice spacing, it is time to confront the computations of $\rho^{\mathrm{x}}_{\epsilon}(E)$ with the exact spectral density $\rho(\omega)$ (comprised of the two-, four-, and six-particle contributions) smeared with the exact

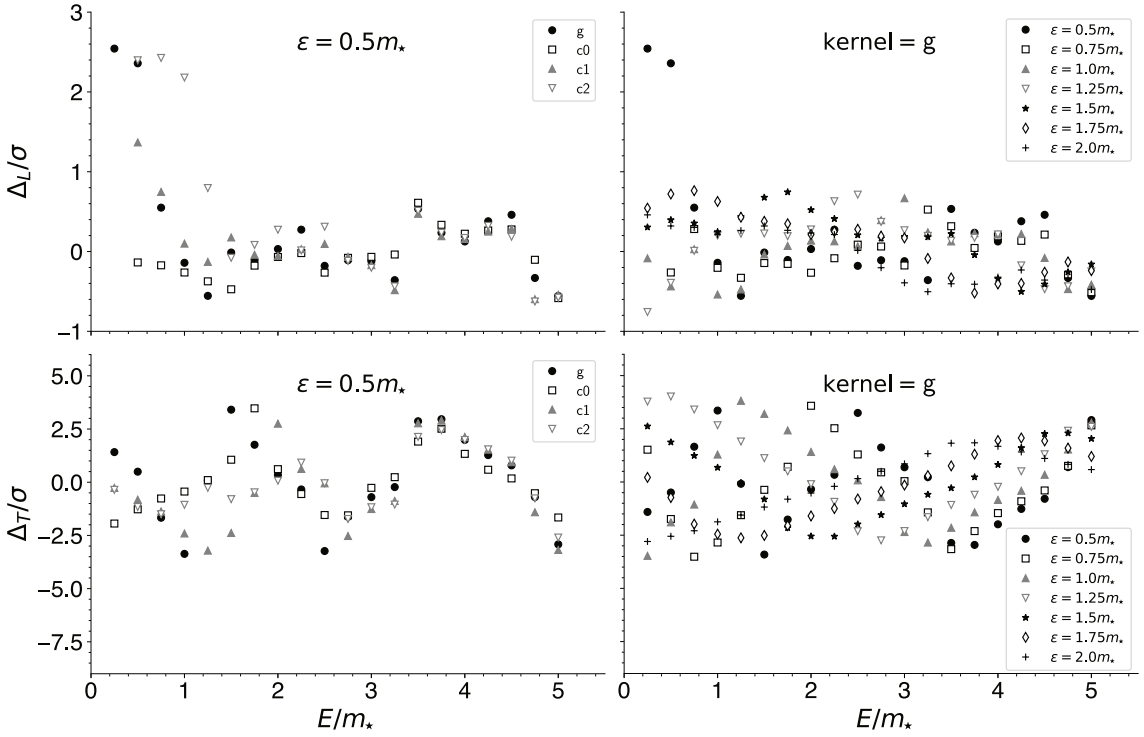

Figure 3: The difference $\Delta_{L,T}$ between spectral reconstruction on ensembles using L and $2L$ (top row), and using ensembles with T and $2T$ in the bottom row. In both cases $\Delta_{L,T}$ is divided by the statistical error on the smaller ensemble. Perhaps some marginally significant hints for finite-L effects are observed at small E near the two-particle production threshold.

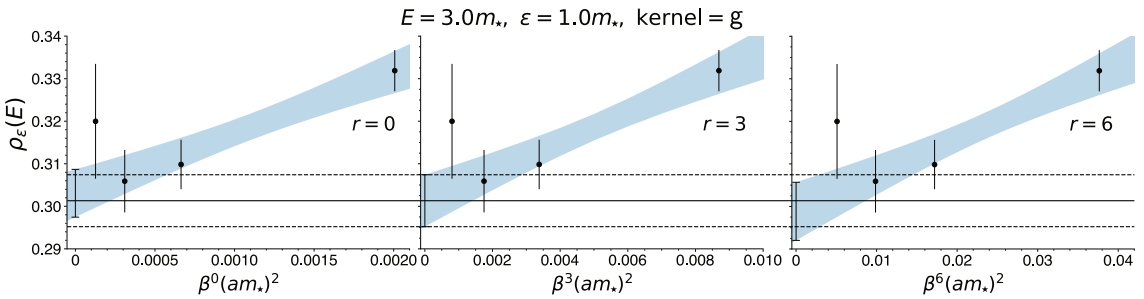

Figure 4: The continuum limit for a single E, ϵ, and smearing kernel using the ansatz of Eq. 13. The shaded band indicates the fit, and the horizontal dotted region the extrapolated value for $r = 3$, which is taken as the final result.

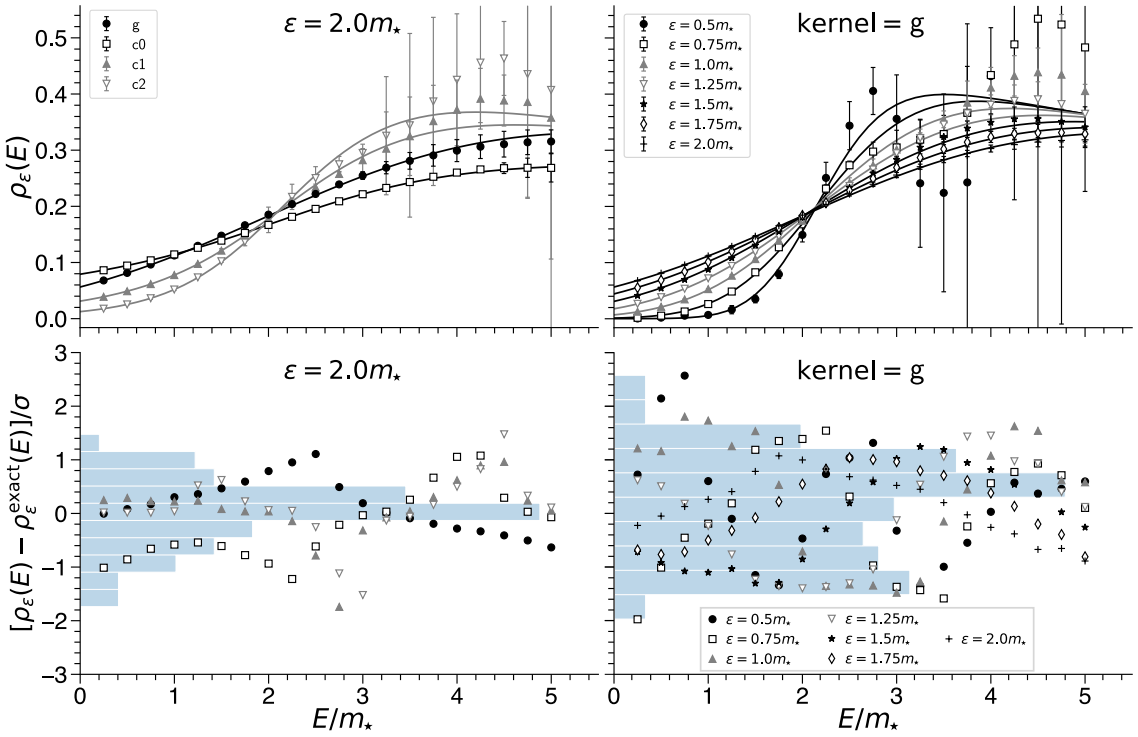

Figure 5: Lattice results for $\rho_\epsilon^{\mathrm{x}}(E)$ in the continuum limit (the data points shown in the legend) compared against the exact spectral density including two-, four-, and six-particle contributions smeared with the exact kernel $\delta_\epsilon^{\mathrm{x}}(E-\omega)$. The exact results are shown as lines in the top row, and the bottom row shows the 'pull' between the numerical data and the exact result, divided by the statistical and systematic error combined in quadrature. A naive histogram of the differences, which ignores correlations among the data, is shown horizontally in the bottom row and approximately resembles the unit gaussian.

smearing kernel $\delta_\epsilon^{\mathrm{x}}(E-\omega)$. Such a comparison is performed in Fig. 5 where the numerical computations are demonstrably consistent with the exact results, within the quoted errors. These errors take into account the statistical errors due to the reconstruction, with any residual systematic errors from finite-L,T effects and the continuum limit added in quadrature.

At this point the verification of the spectral reconstruction approach of Ref. [10] is complete. Smeared spectral densities in the two-dimensional O(3) sigma model have been reconstructed with smearing kernels specified *a priori*, which are consistent with the exact result after the continuum limit has been taken. Consider now the $\epsilon \to 0$ limit in Eq. 5. For this, an important property of the unsmeared spectral density evident in Fig. 1 is required, namely that it varies increasingly slowly with increasing E. This circumvents the limitations in reconstructing kernels with a fixed ϵ and increasing E evident in Fig. 5: larger smearing widths are sufficient at larger E. To this end, the smearing width is scaled $\epsilon \propto (E-2m)$. Also, rather than using a single smearing kernel, $\rho_\epsilon^{\mathrm{x}}(E)$ for all kernels are used to perform constrained extrapolations. For this the small-ϵ expansion is useful

$$\rho_\epsilon^{\mathrm{x}}(E) \equiv \int_0^\infty d\omega\, \delta_\epsilon^{\mathrm{x}}(E-\omega)\,\rho(\omega) = \rho(E) + \sum_{k=1}^{\infty} w_k^{\mathrm{x}} a_k(E)\epsilon^k\,, \tag{14}$$

x	w_k^{x}, even k	w_k^{x}, odd k	w_1^{x}	w_2^{x}	w_3^{x}	w_4^{x}
g	$\frac{k!}{(-2)^{k/2}(k/2)!}$	0	0	−1	0	3
c0	1	1	1	1	1	1
c1	$(1-k)$	$(1-k)$	0	−1	−2	−3
c2	$\frac{1}{3}(k-3)(k-1)$	$\frac{1}{3}(k-3)(k-1)$	0	−1/3	0	1

Table 1: The kernel-dependent coefficients w_k^{x} appearing in the small-ϵ expansion of Eq. (14). For the c1 and c2 kernels, w_3^{c1} and w_5^{c2} (respectively) are the non-zero coefficients with lowest odd order.

where the contribution at the kth order in ϵ is the product of a kernel-independent factor

$$a_k(E) = \begin{cases} \frac{(-1)^{k/2}}{k!}\left(\frac{d}{dE}\right)^k \rho(E)\,, & k \text{ even} \\ \lim_{\eta\to 0^+} \frac{(-1)^{(k-1)/2}}{2\pi}\int_{-\infty}^{\infty} \mathrm{d}\omega\, \frac{\rho(E+\omega)+\rho(E-\omega)}{(\omega+i\eta)^{k+1}}\,, & k \text{ odd} \end{cases} . \tag{15}$$

which depends on the unsmeared spectral density, and a kernel-independent piece $w_k^{(\mathsf{x})}$ which is however independent of $\rho(\omega)$. The $w_k^{(\mathsf{x})}$ for the kernels used here are given for all orders in Tab. 1. The c0 kernel is however not practically useful in such extrapolations due to the $\mathrm{O}(\epsilon)$ term.

A representative constrained extrapolation, in which all kernels (apart from c0) are used to fit for $\rho(E)$ and the $a_k(E)$ up to a certain order, is shown in Fig. 6. A final estimate for $\rho(E)$ is chosen with a statistical error larger than the variation between different extrapolation orders and ranges. Repeating this procedure for all values of E yields the final results for the spectral density $\rho(E)$ shown in Fig. 10. Not only do the numerical results agree with the exact spectral density including two-, four-, and six-particle contributions, but differ significantly from the two-particle contribution alone, indicating the sensitivity to four-particle states. Furthermore, the largest energy of $E = 40m$ is statistically consistent with the two-loop perturbative result, demonstrating that $\rho(E)$ has been computed up to the onset of the perturbative regime.

3. Prospects for QCD

It is in principle straightforward to adopt the analyis of the O(3) sigma model in Sec. 2 to the lattice QCD computation of current spectral densities. However, while it is difficult to compare the density of finite-volume states in one and three spatial dimensions, the O(3) model setup with $mL \approx 30$ may be difficult to achieve in QCD. Fortunately, the masterfield paradigm [15–17] offers the possibility of large lattice volumes by accumulating statistics from widely-separated space-time regions rather than widely-separated Markov chain elements.

Work in this direction has been detailed at this conference in talks by M. Cè and P. Fritzsch. This section describes preliminary work toward the spectral reconstruction of the isovector vector

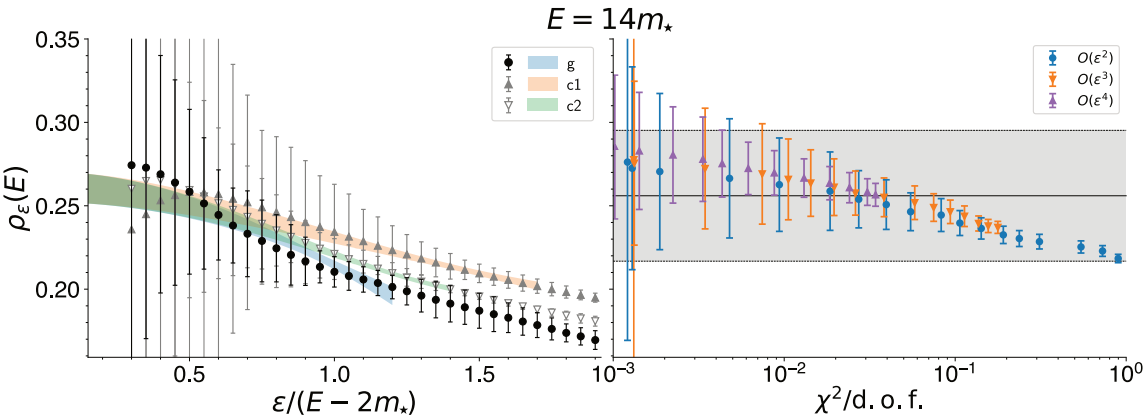

Figure 6: Left: a sample constrained extrapolation using the known coefficients in Tab. 1 up to and including $O(\epsilon^4)$ terms for a fixed energy $E = 14m$. The relative fit ranges of the different smearing kernels are adjusted so that each kernel has an equal amount of support between the two-particle threshold $2m$ and E. **Right**: variation of the extrapolated value of $\rho(E)$ for different extrapolation ranges and orders. The final result is conservatively taken as the horizontal shaded region.

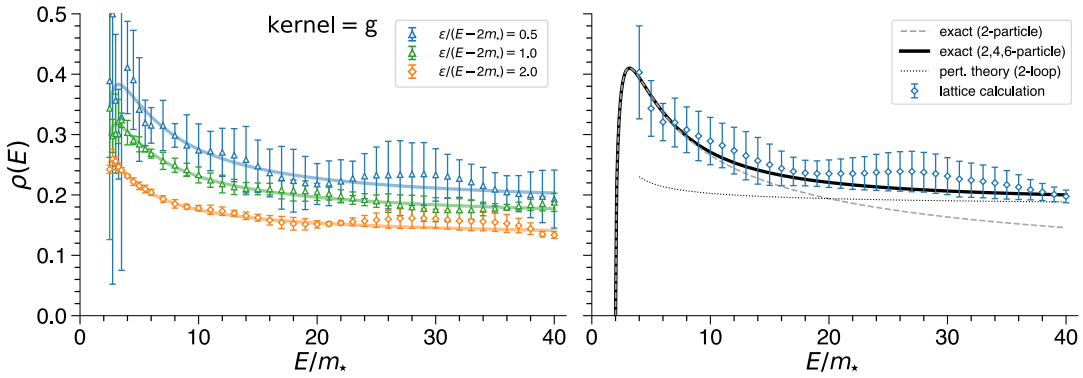

Figure 7: Left: a selection of some of values of ϵ (given in the legend) used in the $\epsilon \to 0$ extrapolation, together with the exact smeared spectral density shown as solid lines for the gaussian kernel. **Right**: the final extrapolated results for $\rho(E)$ together with the exact two-particle contribution to the spectral density and the sum of the two-, four-, and six-particle contributions. The two-loop perturbative spectral density is also shown.

current spectral density with the collaborators and setup mentioned in those talks. Using $N_\mathrm{f} = 2+1$ dynamical flavors of stabilized Wilson fermions [17] at $a = 0.09$ fm, two ensembles were generated with $(L/a)^4 = 96^4$ and 192^4. The analysis described below is based on two and five thermalized, widely separated configuations on the $L/a = 96$ and 192 ensembles, respectively. Details about the construction of the correlators and the estimation of the statistical errors were given by M. Cè. For the data presented here, a variant of the bootstrap procedure is employed.

As suggested in Sec. 1, the prototypical QCD analogue of Sec. 2 is the hadronic component to $e^+e^- \to$ hadrons, which can be obtained by solving the inverse problem of the euclidean current-current correlator projected onto zero spatial momentum in Eq. 3. However, including both the isoscalar and isovector components of the electromagnetic current requires valence quark-line

disconnected Wick contractions, incurring additional computational cost and statistical variance. Consider then the simpler case of the isovector-vector correlator. Phenomenologically this spectral density can be accessed directly from hadronic decays of the tau lepton [18]. A state-of-the-art phenomenological determination of the isovector-vector spectral density is performed in Ref. [19].

The spectral reconstruction approach of Sec. 2 is adopted nearly identically here, apart from some key differences. First, the basis functions provided by the correlator data in Sec. 2 are $b_t(\omega) = \mathrm{e}^{-\omega t} + \mathrm{e}^{-\omega(T-t)}$, but those employed in this analysis from Eq. 3 are $b_t(\omega) = \omega^2\,\mathrm{e}^{-\omega t}$. The flexibility of the formalism of Sec. 2 to handle these different basis functions is an advantage over the Chebyshev approach of Ref. [7]. Also, for these large lattices the finite temporal extent can be demonstrably ignored. For a first test of the approach in QCD, only the gaussian smearing kernel from Eq. 9 is considered. All correlator timeslices from $t_{\mathrm{min}} = a$ to $t_{\mathrm{max}} = 35a$ are used in the reconstruction, and all arithmetic operations are performed with 400 bits of computer precision using the `Arb` library [20].

Another innovation for this analysis compared to Sec. 2 is the procedure for choosing the λ at which statistical errors dominate the systematic errors. As suggested by the left panel in Fig. 2, the procedure in Sec. 2 which balances the two functionals $A[g]/A[0]$ and $B[g]$ from Eq. 11 is perhaps over-conservative and somewhat arbitrary. The alternative approach employed here makes use of one of the possible constraints introduced in Ref. [11]. By the addition of a lagrange multiplier, it is possible to enforce constraints on the reconstructed smearing kernel $\hat{\delta}^{\mathsf{g}}_{\epsilon}(E,\omega)$. Ref. [11] describes how to impose the coincidence of the reconstructed and desired kernels at a particular point

$$\hat{\delta}^{\mathsf{g}}_{\epsilon}(E,\omega^*) = \delta^{\mathsf{g}}_{\epsilon}(E-\omega^*). \tag{16}$$

Although Ref. [11] only considers $\omega = E$, the generalization to arbitrary ω^*, even outside the interval $[E_0,\infty)$, is straightforward.

Using this 'equal value' constraint on the reconstructed kernel, it is possible to estimate how small $A[g]/A[0]$ must be for the statistical errors to dominate. An 'ensemble' of reconstructions are performed with different values of ω^*, in addition to the unconstrained one. The systematic error estimate is then obtained from the variation of $\hat{\rho}^{\mathsf{g}}_{\epsilon}(E)$ among this ensemble at similar $A[g]/A[0]$. The point at which this variation is smaller than the statistical error on the unconstrained result is taken as the optimal reconstruction. Of course this procedure depends on the ensemble of constraint points $\{\omega^*\}$ which are considered. However, it is sensitive the unsmeared spectral density $\rho(\omega)$, in contrast to the approach of Ref. [11]. If additional values of ω^* are added for which $\rho(\omega^*)$ has little support, these will likely differ little from the unconstrained case, apart from possible variations in $\hat{\delta}^{\mathsf{g}}_{\epsilon}(E,\omega)$ away from ω^* induced by the constraint at ω^*. An illustration of this procedure is given in Fig. 8.

After applying the procedure discussed above for a variety of ϵ and E for the gaussian kernel on each of the $L = 9\,\mathrm{fm}$ and $18\,\mathrm{fm}$ ensembles, finite volume effects can be examined. This is done in Fig. 9, using $v_1(s) = 2\pi^2\rho(s)$ for a variety of energies at two different values of the smearing width ϵ. While there are possibly hints of finite-volume effects at the one-to-few sigma level at both ϵ, these effects are generally under control. Additional volumes will however elucidate the situation in the future.

We finally turn to a comparison of the reconstructed isovector vector spectral density with experiment [21]. For this a preliminary value of the vector current renormalization factor Z_V is

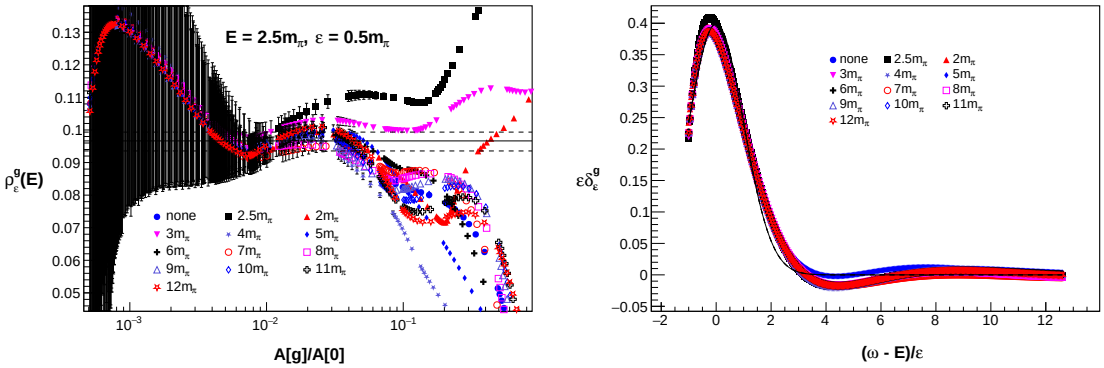

Figure 8: Illustration of the method for choosing the optimal tradeoff parameter λ described in the text for the gaussian reconstruction on the $L = 18$ fm ensemble with $\epsilon = 0.5m_\pi$ and $E = 2.5m_\pi$. **Left**: different values of λ for the unconstrained reconstruction and reconstructed kernels constrained to agree with $\delta^g_\epsilon(E - \omega^*)$ at the various values of ω^* indicated in the legend. The horizontal band indicates the chosen estimate for which the statistical error on the unconstrained reconstruction covers the spread given by the ensemble of constraints. For comparison, the method for balancing statistical and systematic errors of Sec. 2 (and Ref. [11]) chooses the unconstrained point with $A[g]/A[0] \approx 0.0016$. **Right**: the reconstructed smearing kernel compared to the desired gaussian (solid line) for each member of the constraint ensemble near the chosen value of $A[g]/A[0]$ indicated by the horizontal band in the left plot. The residual variation between the different constraints is evidently smaller than the statistical error on the constrained reconstruction, although perhaps additional values of ω^* near $\omega^* - E \approx 2\epsilon$ should be added in the future.

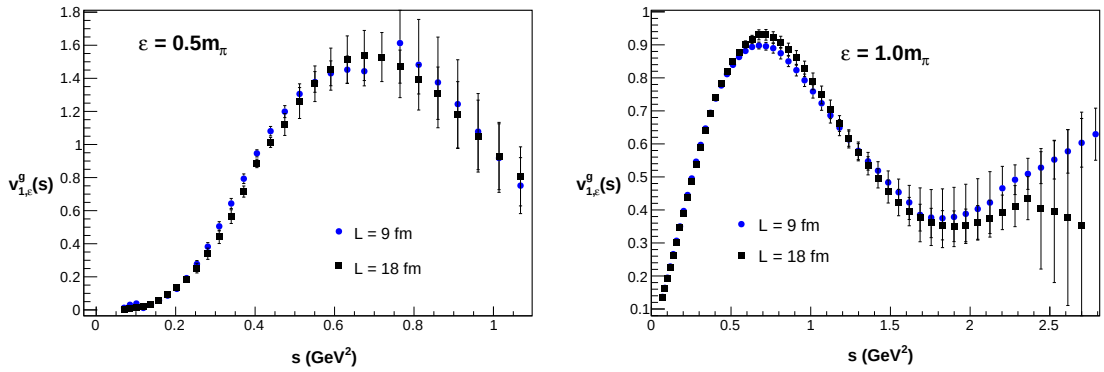

Figure 9: Finite volume effects in the reconstructed vector isovector spectral density on the two masterfield ensembles described in the text. Gaussian smearing is used for a variety of energies at smearing width $\epsilon = 0.5m_\pi$, shown on the left, and $\epsilon = m_\pi$, shown on the right. These effects are generally small apart from some mild discrepancies near $s = 0.4\,\mathrm{GeV}^2$ for $\epsilon = 0.5m_\pi$ and $s = 0.75\mathrm{GeV}^2$ for $\epsilon = m_\pi$. Additional smaller lattice volumes could further examine these potential finite volume effects.

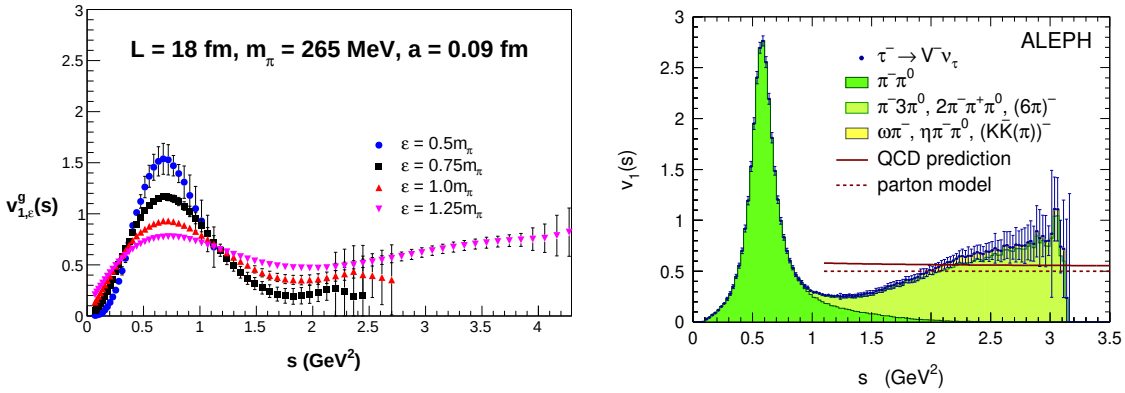

Figure 10: Comparison of the lattice QCD results for the isovector vector spectral density on the larger $L/a = 192$ master field ensemble discussed in the text (shown on the left), with experimental results for hadronic τ-decays on the right. Statistical errors due to the scale setting and the renormalization of the vector current are not yet taken into account.

employed, which was presented at this conference by J. Kuhlmann. The statistical error on Z_V is ignored in these preliminary results, as is the error on the lattice scale, which is crudely set by assuming $m_\pi = 265\,\text{MeV}$. The results are summarized in Fig. 10, and broadly resemble the expermintal plot, with a narrow peak likely due to the $\rho(770)$ vector resonance followed by a slow rise due to four-particle states. Particularly interesting is the mild indication of this rise in the lattice QCD data, which (like in the O(3) model) show the effects of four-pion states. It should be noted that the current state-of-the-art for the finite-volume approach to lattice QCD scattering amplitudes is the numerical computation of (exclusive rather than inclusive) three-pion scattering amplitudes[3].

4. Conclusions

Alternative techniques are required to compute phenomena arising from many hadronic states. The spectral reconstruction of smeared spectral densities from euclidean correlator data not only bridges the gap between finite- and infinte-volume, but also helps to regulate the ill-posed nature of the problem. The appilcation discussed here is the computation of inclusive rates summed over all final states produced by an external current. In the two-dimensional O(3) model, after taking the continuum limit, the algorithm presented in Sec. 2 (first proposed for lattice field theory in Ref. [10]) results in smeared spectral densities consistent with known analytic results. Spectral reconstruction algorithms based on the Backus-Gilbert approach [5, 6] enable a precise definition of the smeared spectral density that has been computed, while the modification of Ref. [9] further allows the *a priori* specification of a desired smearing kernel. The simple linear ansatz on which these approaches are based enables the direct expression for the smearing kernel given in Eq. 6.

Smeared spectral densities are useful not only for inclusive decay rates. An incomplete list of recent applications of the Backus-Gilbert approach includes the nucleon hadronic tensor [24],

[3]For a review of the current status of computations of three-particle scattering amplitudes using the finite-volume approach, see the presentation by F. Romero-López and the recent reviews in Refs. [22, 23].

the determination of PDFs from Ioffe time data [25], and the photon emissivity of the quark-gluon plasma [26]. These applications do not employ the algorithmic variant enabling *a priori* specification of the smearing kernel, but could perhaps benefit from it in the future. This *a priori* specification of the kernel enabled in Refs. [9, 10] is also present in the Chebshev approach of Ref. [7], but the stabilizing effect of the functional $B[g]$ in Eq. 11 is naively not present. The work of Ref. [8] is a first step towards comparing the two approaches.

The advantages of the *a priori* approach are leveraged in the two-dimensional O(3) model to perform joint constrained $\epsilon \to 0$ extrapolations with several different kernels. The presence of the narrow $\rho(770)$ peak in the isovector vector spectral density in QCD discussed in Sec. 3 complicates such an extrapolation and more work is required toward an implementation. A similar approach has been employed to compute inclusive decay rates in Refs. [27, 28], and taken up by additional groups in Refs. [8, 29, 30]. Work towards computing the R-ratio was reported in this conference by A. De Santis, as well as similar analyses of the total hadronic tau decay rate [31–33], albeit with a wider gaussian smearing radius than employed here. Furthermore, the *a priori* approach of Ref. [7] led to the direct computation of the Borel transform of a current-current correlator required for the Shifman-Vainshtein-Zakharov sum rule in Ref. [34], possibly opening the door for additional interaction between lattice QCD and QCD sum rules. Another interesting application is pursued in Ref. [35] in which fits to smeared spectral densities are considered as an alternative to 'standard' spectroscopy. Additional applications could appear in the future. The *a priori* approach in principle enables the computation of exclusive scattering amplitudes using Refs. [36, 37], while the formalism for inclusive rates was developed already in Refs. [3, 38].

References

[1] A. Pich, *Precision physics with inclusive QCD processes*, *Prog. Part. Nucl. Phys.* **117** (2021) 103846, [arXiv:2012.04716].

[2] E. C. Poggio, H. R. Quinn, and S. Weinberg, *Smearing the Quark Model*, *Phys. Rev. D* **13** (1976) 1958.

[3] M. T. Hansen, H. B. Meyer, and D. Robaina, *From deep inelastic scattering to heavy-flavor semileptonic decays: Total rates into multihadron final states from lattice QCD*, *Phys. Rev. D* **96** (2017), no. 9 094513, [arXiv:1704.08993].

[4] O. Kaczmarek and H.-T. Shu, *Spectral and Transport Properties from Lattice QCD*, *Lect. Notes Phys.* **999** (2022) 307–345, [arXiv:2206.14676].

[5] G. Backus and F. Gilbert, *The resolving power of gross earth data*, *Geophysical Journal International* **16** (1968), no. 2 169–205.

[6] G. Backus and F. Gilbert, *Uniqueness in the inversion of inaccurate gross earth data*, *Philosophical Transactions of the Royal Society of London A: Mathematical, Physical and Engineering Sciences* **266** (1970), no. 1173 123–192, [http://rsta.royalsocietypublishing.org/content/266/1173/123.full.pdf].

[7] G. Bailas, S. Hashimoto, and T. Ishikawa, *Reconstruction of smeared spectral function from Euclidean correlation functions*, *PTEP* **2020** (2020), no. 4 043B07, [arXiv:2001.11779].

[8] A. Barone, S. Hashimoto, A. Jüttner, T. Kaneko, and R. Kellermann, *Inclusive semi-leptonic $B_{(s)}$ mesons decay at the physical b quark mass*, in *39th International Symposium on Lattice Field Theory*, 11, 2022. arXiv:2211.15623.

[9] F. Pijpers and M. Thompson, *Faster formulations of the optimally localized averages method for helioseismic inversions*, *Astronomy and Astrophysics* **262** (08, 1992) L33–L36.

[10] M. Hansen, A. Lupo, and N. Tantalo, *Extraction of spectral densities from lattice correlators*, *Phys. Rev. D* **99** (2019), no. 9 094508, [arXiv:1903.06476].

[11] J. Bulava, M. T. Hansen, M. W. Hansen, A. Patella, and N. Tantalo, *Inclusive rates from smeared spectral densities in the two-dimensional O(3) non-linear σ-model*, *JHEP* **07** (2022) 034, [arXiv:2111.12774].

[12] M. Luscher and U. Wolff, *How to Calculate the Elastic Scattering Matrix in Two-dimensional Quantum Field Theories by Numerical Simulation*, *Nucl. Phys.* **B339** (1990) 222–252.

[13] J. Balog and M. Niedermaier, *Off-shell dynamics of the O(3) NLS model beyond Monte Carlo and perturbation theory*, *Nucl. Phys. B* **500** (1997) 421–461, [hep-th/9612039].

[14] J. Balog, F. Niedermayer, and P. Weisz, *The Puzzle of apparent linear lattice artifacts in the 2d non-linear sigma-model and Symanzik's solution*, *Nucl. Phys. B* **824** (2010) 563–615, [arXiv:0905.1730].

[15] M. Lüscher, *Stochastic locality and master-field simulations of very large lattices*, *EPJ Web Conf.* **175** (2018) 01002, [arXiv:1707.09758].

[16] L. Giusti and M. Lüscher, *Topological susceptibility at $T > T_c$ from master-field simulations of the SU(3) gauge theory*, *Eur. Phys. J. C* **79** (2019), no. 3 207, [arXiv:1812.02062].

[17] A. Francis, P. Fritzsch, M. Lüscher, and A. Rago, *Master-field simulations of O(a)-improved lattice QCD: Algorithms, stability and exactness*, *Comput. Phys. Commun.* **255** (2020) 107355, [arXiv:1911.04533].

[18] M. Davier, A. Hocker, and Z. Zhang, *The Physics of Hadronic Tau Decays*, *Rev. Mod. Phys.* **78** (2006) 1043–1109, [hep-ph/0507078].

[19] D. Boito, M. Golterman, K. Maltman, S. Peris, M. V. Rodrigues, and W. Schaaf, *Strong coupling at the τ-mass scale from an improved vector isovector spectral function*, in *16th International Workshop on Tau Lepton Physics* , 12, 2021. arXiv:2112.05413.

[20] F. Johansson, *Arb: efficient arbitrary-precision midpoint-radius interval arithmetic*, *IEEE Transactions on Computers* **66** (2017) 1281–1292.

[21] **ALEPH** Collaboration, S. Schael et al., *Branching ratios and spectral functions of tau decays: Final ALEPH measurements and physics implications*, *Phys. Rept.* **421** (2005) 191–284, [hep-ex/0506072].

[22] M. T. Hansen and S. R. Sharpe, *Lattice QCD and Three-particle Decays of Resonances*, *Ann. Rev. Nucl. Part. Sci.* **69** (2019) 65–107, [arXiv:1901.00483].

[23] M. Mai, U.-G. Meißner, and C. Urbach, *Towards a theory of hadron resonances*, arXiv:2206.01477.

[24] **XQCD** Collaboration, J. Liang, T. Draper, K.-F. Liu, A. Rothkopf, and Y.-B. Yang, *Towards the nucleon hadronic tensor from lattice QCD*, *Phys. Rev. D* **101** (2020), no. 11 114503, [arXiv:1906.05312].

[25] J. Karpie, K. Orginos, A. Rothkopf, and S. Zafeiropoulos, *Reconstructing parton distribution functions from Ioffe time data: from Bayesian methods to Neural Networks*, *JHEP* **04** (2019) 057, [arXiv:1901.05408].

[26] M. Cè, T. Harris, A. Krasniqi, H. B. Meyer, and C. Török, *Photon emissivity of the quark-gluon plasma: A lattice QCD analysis of the transverse channel*, *Phys. Rev. D* **106** (2022), no. 5 054501, [arXiv:2205.02821].

[27] P. Gambino, S. Hashimoto, S. Mächler, M. Panero, F. Sanfilippo, S. Simula, A. Smecca, and N. Tantalo, *Lattice QCD study of inclusive semileptonic decays of heavy mesons*, *JHEP* **07** (2022) 083, [arXiv:2203.11762].

[28] P. Gambino and S. Hashimoto, *Inclusive Semileptonic Decays from Lattice QCD*, *Phys. Rev. Lett.* **125** (2020), no. 3 032001, [arXiv:2005.13730].

[29] R. Kellermann, A. Barone, S. Hashimoto, A. Jüttner, and T. Kaneko, *Inclusive semi-leptonic decays of charmed mesons with Möbius domain wall fermions*, in *39th International Symposium on Lattice Field Theory*, 11, 2022. arXiv:2211.16830.

[30] P. Gambino, S. Hashimoto, S. Mächler, M. Panero, F. Sanfilippo, S. Simula, A. Smecca, and N. Tantalo, *Inclusive semileptonic B-decays from lattice QCD*, in *39th International Symposium on Lattice Field Theory*, 11, 2022. arXiv:2211.11833.

[31] A. Evangelista, R. Frezzotti, G. Gagliardi, V. Lubicz, F. Sanfilippo, S. Simula, and N. Tantalo, *Direct lattice calculation of inclusive hadronic decay rates of the τ lepton*, in *39th International Symposium on Lattice Field Theory*, 1, 2023. arXiv:2301.00796.

[32] C. Alexandrou et al., *Lattice calculation of the R-ratio smeared with Gaussian kernel*, in *39th International Symposium on Lattice Field Theory*, 12, 2022. arXiv:2212.12493.

[33] C. Alexandrou et al., *Probing the R-ratio on the lattice*, arXiv:2212.08467.

[34] T. Ishikawa and S. Hashimoto, *Spectral sum of current correlators from lattice QCD*, *Phys. Rev. D* **104** (2021), no. 7 074521, [arXiv:2103.06539].

[35] L. Del Debbio, A. Lupo, M. Panero, and N. Tantalo, *Multi-Representation Dynamics of SU(4) Composite Higgs Models: Chiral Limit and Spectral Reconstructions*, arXiv:2211.09581.

[36] J. Bulava and M. T. Hansen, *Scattering amplitudes from finite-volume spectral functions*, *Phys. Rev. D* **100** (2019), no. 3 034521, [arXiv:1903.11735].

[37] M. Bruno and M. T. Hansen, *Variations on the Maiani-Testa approach and the inverse problem*, *JHEP* **06** (2021) 043, [arXiv:2012.11488].

[38] H. Fukaya, S. Hashimoto, T. Kaneko, and H. Ohki, *Towards fully nonperturbative computations of inelastic ℓN scattering cross sections from lattice QCD*, *Phys. Rev. D* **102** (2020), no. 11 114516, [arXiv:2010.01253].